

SkyWindFarm

Harnessing High Altitude Wind Power in a Scalable Manner



Yash Dagade
Power Plasma Propulsion Lab
Prof. Sayan Biswas

Abstract

Wind energy is cubically proportional to wind velocity. As altitude increases, wind velocity not only significantly increases but also becomes more consistent in direction and intensity. However, current airborne wind energy systems (AWES) struggle to harness this stable, untapped resource at scale. SkyWindFarm is the first AWE system capable of harnessing the power of high-altitude winds in a scalable manner. Utilizing vertical axis wind turbines (VAWTs) in a bio-inspired cluster configuration, SkyWindFarm capitalizes on the inherent advantages of VAWTs for airborne applications, such as increased stability and optimal performance in farm configurations. Simulated annealing based CFD optimizations have been conducted to optimize the VAWT cluster, resulting in an overall C_p of 0.47 at TSR 3.0. The system's development has achieved a Technology Readiness Level of 5 through proof-of-concept airborne demonstrations, utilizing a laboratory-scale prototype. Empirical results from wind tunnel testing show a strong alignment (correlation > 0.95) with CFD simulations. Further, a transient 6 Degrees of Freedom simulation reveals that SkyWindFarm can reject even the harshest disturbances in approximately 7 seconds. The study comprehensively addresses all major challenges. A comparative cost analysis reveals that SkyWindFarm outperforms current FlyGen AWEs by 25% in efficiency and offers one of the most competitive levelized costs of energy at 25\$/MWhr. Furthermore, SkyWindFarm design has the emergent capability for rapid adoption, capable of ramping up power production to the megawatt range. SkyWindFarm is also the first AWE system that can serve as a primary power source, bolstering its value for remote communities and marking a crucial stride toward a sustainable future for all.

All images in this manuscript were produced by the author unless otherwise noted.

Note: Contents from this manuscript have been patented and are under publication in the CDPMHM2024, and are currently under peer review in the Renewable Energy Journal. Further SkyWindFarm concept has also been filed for a 500,000\$ DoE grant under the ARPA-E branch.

1. Introduction

Energy supply is a fundamental need for people and communities across the globe, serving our need for safety, clean drinking water, education, and basic business practices, and its demand continues to increase, with predictions of a 50% increase in the next decade alone. A critical challenge facing global supplies is that, humans are consuming natural petroleum at a rate that is 105 times faster than nature can replenish it [1]. According to recent predictions, current coal supplies will only last for about 107 years, crude oil for about 35 years, and natural gas for about 37 years [2]. This dependence on fossil fuels is unsustainable and contributes to global warming by increasing greenhouse gas levels in the atmosphere [3]. To slow or reverse global warming, fossil fuel use must decline with increasing application of renewable, carbon-neutral, and greener fuel source alternatives. Therefore, the search for clean energy has become paramount [4].

Airborne Wind Energy systems(AWEs) have emerged as a revolutionary technology with the capability to harness the energy of high-altitude wind currents [5], [6], [7], [8], [9], [10]. Consequently, AWEs offer the promise of generating electricity at substantially lower costs [11], [12], [13] and with reduced environmental impact compared to conventional ground-based wind turbines.

1.2 Categorization of Airborne Wind Energy Systems

The current landscape of AWEs can be partitioned into two primary categories based on their modality of power generation: intermittent and continuous systems. Intermittent AWEs predominantly utilize ground-anchored generators and exploit gliders to capture and convert aerodynamic forces into electrical energy [14], [15], [16], [17], [18]. In contrast, continuous AWEs [19], [20], [21], [22], [23], [24] facilitate direct conversion of wind energy. This subset of continuous AWEs can be further nuanced into systems designed for lower altitudes, which generally include Crosswind Airborne Wind Energy Systems [25] and Buoyant Airborne Turbines [23], and those engineered for higher altitudes, like the Flying Electric Generator [26]. This paper introduces a novel and innovative concept - SkyWindFarm, which utilizes Vertical Axis Wind Turbines (VAWTs), offering unique advantages over other AWEs. SkyWindFarm is specifically engineered to harness the potential of high-altitude wind energy.

1.3 Wind Patterns

Expanding on the need for sustainable energy solutions, the largely unexplored potential of high-altitude wind patterns deserves special consideration. High altitude winds are an untapped potential for AWEs [5]. As altitude rises, not only does wind velocity increase, but it also becomes more consistent in direction and intensity. To analyze wind speed distribution, one of the widely adopted

$c(h) = c_0 \left(\frac{h}{h_0}\right)^n$	Equation 1
$k(h) = \frac{k_0 \left[1 - 0.088 \ln\left(\frac{h_0}{10}\right) \right]}{\left[1 - 0.088 \ln\left(\frac{h}{10}\right) \right]}$	Equation 2
$n = \frac{[0.37 - 0.088 \ln(c_0)]}{[1 - 0.088 \ln\left(\frac{h}{10}\right)]}$	Equation 3

statistical tools is the Weibull model [27], which is characterized by its shape parameter, $c(h)$, and scale parameter, $k(h)$. These parameters can be expressed as functions of altitude [27], as described by the **Equations 1 and 2**. In the shape parameter, ‘ n ’ in the equation is calculated as shown in **Equation 3**.

These equations offer a predictive framework to comprehend wind attributes at different altitudes based on given shape and scale parameters. For the scope of this paper, London, in the United Kingdom is considered as the operational region due to the comprehensive availability of wind data [28]. Using **Equations 1-3** at Station number 11 for altitude of 3000 meters, $c(3000) = 26.7$ and $k(3000) = 6.99$. Nevertheless, it is important to emphasize that the findings are universally applicable. By utilizing Weibull distribution parameters and leveraging data, **Figure 1** is generated to visualize the wind speed characteristics at different altitudes.

An operational altitude of 3000 meters is selected, not as a maximum operational threshold, but rather due to the substantial availability of wind data at this altitude. SkyWindFarm is designed to operate effectively at altitudes extending up to 10 kilometers, far surpassing the limits of conventional AWEs.

Weibull analysis reveals a significant increase in wind speeds at an altitude of 3000 meters. Here, wind

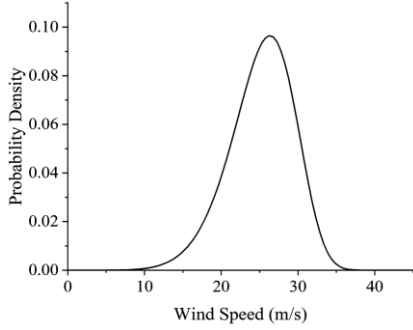


Figure 1. Probability density of wind speed for 3000 meters altitudes

speeds are observed to lie between 18 to 33 m/s for over 90% of the time, with a mean wind speed of 26.7 m/s. The Weibull model for wind speed aligns with the historically average wind speed above Central London [11], as can be seen from extrapolating **Figure 2**. Hence, for the subsequent simulations and calculations in this study, wind speed of 26.7 m/s and an air density of 0.8 kg/m³ are used.

Given the inherent advantage of elevated wind patterns, SkyWindFarm specifically targets subtropical jet streams characterized by high wind speeds. As wind power is cubically proportional to wind speed, the benefits of operating at these elevated altitudes are considerable. Traditional AWEs technologies, although airborne, are typically constrained to low-altitude operations. This limitation not only restricts their energy-generating capacity, but also inflates operational costs and raises safety concerns, further exacerbating the Not in My Backyard syndrome [29] leading to lower adoption.

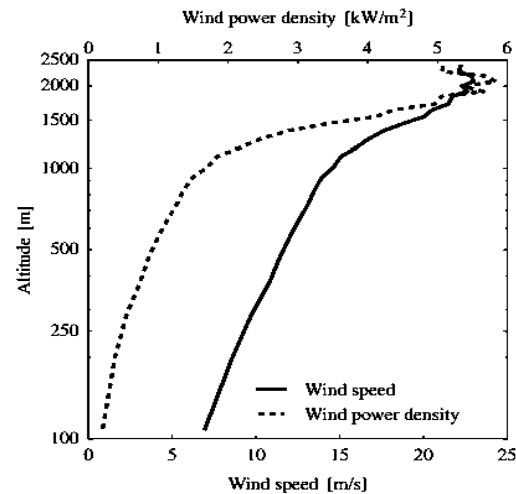


Figure 2 Average Wind speed above Central London [11]

1.4 Vertical Axis Wind Turbines for Airborne Operations

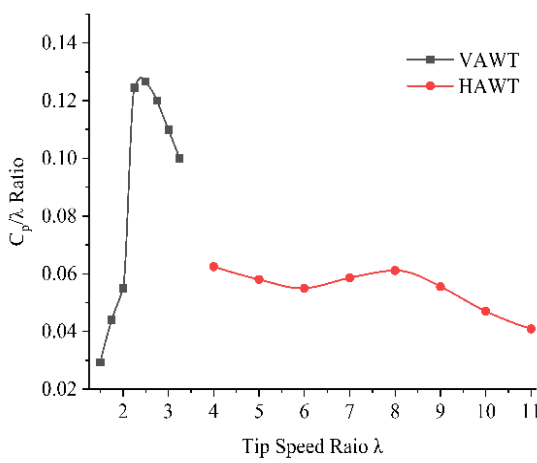


Figure 3. Tip speed ratio v/s Coefficient of Power/Tip speed ratio for VAWT and HAWT

Building upon the insights into high-altitude wind patterns, the technological choice of wind turbines for airborne applications becomes paramount. VAWTs emerge as a particularly favorable technology over Horizontal Axis Wind Turbines (HAWTs) for several reasons, especially in the context of harnessing high altitude airborne winds.

VAWTs offer unique advantages in farm configurations, notably superior energy density and efficiency compared to HAWTs. While a standalone VAWT may underperform a lone HAWT in terms of efficiency, a cluster of VAWTs exhibits markedly

superior performance [30], [31]. Additionally, their inherent stability and quieter operation make them particularly well-suited for airborne applications where dynamic stability and noise minimization are crucial [32]. Furthermore, VAWTs offer the added benefit of achieving higher power coefficients C_p at lower Tip-Speed Ratios (TSR). The ratio of C_p to TSR has critical importance in high-wind-speed environments, as elevated TSR levels can introduce structural challenges and compromise system integrity. Additionally, higher TSRs would induce greater noise and vibrations, thereby leading to vortex-induced vibrations, which can increase the tether drag by over 300% [33]. **Figure 3** showcases this advantage, illustrating the favorable C_p to TSR ratio of VAWTs [34] compared to HAWTs [35].

An often-overlooked attribute of VAWTs is their compatibility with diffusers and guide vanes [36], [37], [38], [39]. Incorporating these features into a Diffuser Augmented VAWT (DAWT) significantly improves its performance coefficients without a substantial increase in mass, making it an optimal choice for airborne systems where weight is a critical factor.

Considering these factors, this research introduces a pioneering concept called SkyWindFarm, specifically designed to leverage the distinctive benefits of VAWT clusters at high altitudes. SkyWindFarm is engineered to be scalable in the Megawatt range, making it capable of adapting to varying energy demands, even in remote regions with low population density. This innovative non-crosswind scalable design is developed to tackle the challenges posed by conventional AWEs, offering a resilient and expandable approach to tapping into high-altitude wind energy. As such, it presents a promising solution within the renewable energy sector.

2 SkyWindFarm

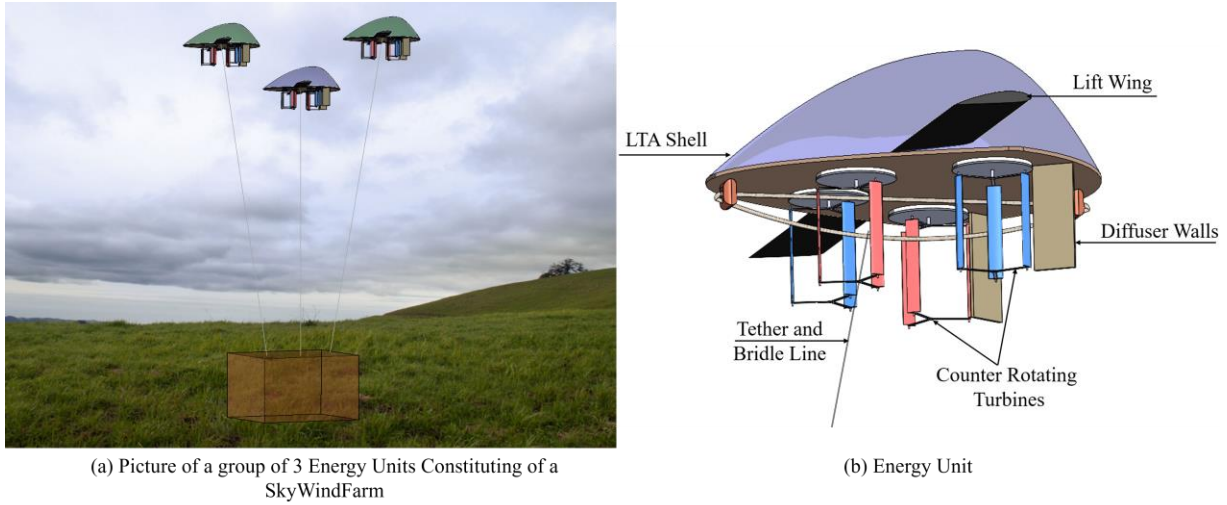


Figure 4. SkyWindFarm

SkyWindFarm is specifically engineered to exploit the high wind speeds commonly observed in major atmospheric circulations such as sub-tropical and polar jet streams [38]. Unlike traditional AWEs that operate at low altitudes, SkyWindFarm is designed to function at elevations where wind power density is the most potent. The design's scalability ensures that it can adapt to fluctuating energy demands, making it particularly relevant for remote or sparsely populated regions. A SkyWindFarm as shown in **Figure 4a** is composed of one or more Energy Units, with each unit featuring a cluster of four counter rotating VAWTs. The configuration of these Energy Units is flexible, allowing for optimal positioning in the airspace to maximize each unit's energy output.

2.1 Energy Unit: Design

Each Energy Unit as shown in **Figure 4b** serves as a multifunctional platform consisting of five primary components: the VAWT cluster, a lighter-than-air (LTA) shell, an aerodynamic wing, a bridle line system, and an electricity-conducting tether.

2.1.1 VAWT Cluster

The VAWT cluster comprises of four three-bladed counter rotating Darrius wind turbines. The turbine's outer structure is designed using a carbon fiber composite characterized by a high modulus of elasticity, typically around 290 GPa, with a density of approximately 1.82 g/cm^3 [40]. This choice ensures optimal strength-to-weight ratios, crucial for airborne applications. The inner protective layer is fabricated from a hydrophobic fabric, specifically chosen to provide resistance against potential water damage, be it from cloud moisture or precipitation. The use of hydrophobic fabric also ensures protection against icing.

Carbon fibers themselves are resistant to radiation damage, but the resins that bind the fibers together can degrade over time when exposed to ultraviolet radiation. However, UV protection coating systems can help prevent[41] this problem and expand the life of turbine, extending the operational life of Energy Unit.

The choice of material ensures that the turbine operates at high RPMs while maintaining a lightweight structure. Additionally, the turbines are designed to function at cutout wind speeds of up to 60 meters per second.

Generators

Each turbine features air-core Permanent Magnet Direct Drive (PMDD) generators, selected for their lightweight construction and high efficiency. These attributes make PMDDs well-suited for the challenging environment of high-altitude wind energy harvesting [23]. Using a composite material and PMDD generators, the total mass of one turbine is calculated to be approximately 300kg.

2.1.2 Lighter-than-air (LTA) shell

SkyWindFarm uses helium as an LTA gas for lift. The aerodynamic shape for SkyWindFarm is constructed through specialized support structure that are both light in weight while providing a robust structure. LTA shell is under near constant load from the internal pressure and must withstand the UV radiation and other environmental effects. The construction of the LTA shell incorporates several layers, each with a specific function. On the exterior, Polyvinyl Fluoride (PVF), serves as an environmental barrier, safeguarding against weather and ultraviolet radiation. Beneath this, a Polyester film acts as a helium barrier, essential for maintaining the shell's buoyancy by preventing the gas from seeping out. This barrier can ensure helium stays in for as long as 2 years without needing a refill. The core structure is provided by a woven polyester base cloth, which imparts the necessary tensile strength and durability. The inner surface is coated with a thermoplastic urethane layer, which allows for effective heat sealing, ensuring the structural integrity of the shell by bonding the layers together securely.

2.1.3 Aerodynamic wing

The aerodynamic wing is made of a hydrophobic fabric coating on the outside and is hollow on the inside, inspired by the model airplane wings. The wing structure is made for durability. It consists of carbon fiber reinforcement structures. Additionally, the wings are designed to actuate rapidly and seamlessly to adjust the angle of attack in response to changing wind speeds.

2.1.4 Tether and Bridle Line System

The SkyWindFarm design ensures altitude control through an integrated system comprising a Lift Wing and a Tether and Bridle Line mechanism. Unlike crosswind systems, which frequently encounter significant tether tensions [42], SkyWindFarm tether remains static, resulting in comparatively low tether tensions. Furthermore, the SkyWindFarm uses an electrical conduction tether capable of transmitting electricity efficiently over long distances, proven in applications reaching 5km [26].

2.2 Energy Unit: Features

In developing the SkyWindFarm Energy Unit, specific challenges unique to high-altitude wind energy systems were identified. To guarantee robust and efficient functioning, targeted mitigation strategies were

incorporated into the design. A notable example is the deployment of counter-rotating turbines, which not only achieve net zero angular momentum but also enhance the farm's power output. Below are some key challenges and their respective mitigation strategies:

2.2.1 Operation of the Energy Unit

Designed for long-term, autonomous operation at high altitudes, each Energy Unit in the SkyWindFarm undergoes an initial towing phase to reach its designated operational altitude. Once airborne, the farm employs a dual lift strategy that combines both aerostatic and aerodynamic lift mechanisms. This feature allows the farm to maintain or adapt its altitude with high efficiency, optimizing its position relative to high-density wind layers. Upon attaining the desired altitude, the VAWT clusters within each Energy Unit start converting the kinetic energy of the wind into electrical energy. This energy is then transferred to the ground through a specialized, electricity conductive tether, facilitating immediate integration into the existing electrical grid. In cases where the farm needs to descend, SkyWindFarm employs a set of adjustable aerodynamic wings. By dynamically altering the angles of attack of these wings, the system can execute a controlled, gradual descent, ensuring the Energy Unit's secure return to ground level. This operational flexibility enhances SkyWindFarm's suitability for sustained, high-altitude energy capture.

2.2.2 Air Traffic Management

Anti-collision lights, transponders, and Very High Frequency (VHF) radio tools are implemented to ensure safety and coordination with nearby pilots [43]. To mitigate risks to natural air traffic like birds, the system employs stationary operation, limited moving parts, and light and sound-based deterrents. Moreover, the operational altitude of approximately 3 km is beyond the typical range for most bird species, thereby minimizing potential for conflict[44].

2.2.3 Blowdown angle

The blowdown angle arises from the drag faced by the farm, causing its airborne trajectory to follow a slight angle. A high blowdown angle necessitates longer tethers to reach a specific height and consumes substantial airspace, leading to increased projected space required for the AWE system and greater tether transmission losses [23].

The blowdown angle, determined by the ratio of lift to drag, is given by **Equation 4**. The force of lift and drag were calculated from simulations done in the Stability section. SkyWindFarm has one of the lowest operational blowdown angles, around 16 degrees of any AWE system [45], while operating.

3 System Weight and Lift Mechanism Assessment

A cornerstone of the SkyWindFarm design is the meticulous optimization of the system's weight, aimed at maximizing the effectiveness and efficiency of high-altitude energy harvesting. A comprehensive weight assessment has been executed through Computer-Aided Design modeling. This involves the prudent

$$\delta = \arctan\left(\frac{F_d}{F_l}\right) \approx \arctan\left(\frac{4754}{16250}\right) \approx 16 \quad \text{Equation 4}$$

selection of materials and engineering of structural elements to achieve a balance between minimal weight and maximum structural integrity. The primary structure of each Energy Unit is mainly hollow, which significantly contributes to mass reduction. The total weight of one Energy Unit is conservatively approximated to 1.75 tons, serving as the basis for all lift calculations in this study.

3.1 Dual Lift Mechanism

SkyWindFarm integrates both aerostatic and aerodynamic lift mechanisms, offering system stability and operational flexibility. The aerostatic lift is primarily generated through a helium-filled LTA shell, meticulously designed to minimize aerodynamic drag while facilitating passive orientation correction. The inherent stability of this lift mechanism is augmented by maintaining a low center of gravity, thus reducing the risk of system toppling. On the other hand, aerodynamic lift is generated by adjustable wing structures, allowing for dynamic adaptation to varying wind conditions. This dual lift approach ensures stable operation at a predetermined altitude.

3.1.1 Aerostatic Lift Generation

The aerostatic lift is an essential component in the SkyWindFarm architecture, realized through a helium-filled balloon. Helium's inert properties, ease of handling, and intrinsic safety make it the lifting gas of choice. The aerostatic lift force, generated by the helium-filled LTA shell, was computed to be approximately 3750 N, calculated by **Equation 5**; where, V is volume of helium in the LTA shell (600 m^3), ρ_s is the density of surrounding air ($0.8 \frac{\text{kg}}{\text{m}^3}$), and ρ_{eb} is density of helium ($0.179 \frac{\text{kg}}{\text{m}^3}$).

3.1.2 Aerodynamic Lift Contribution

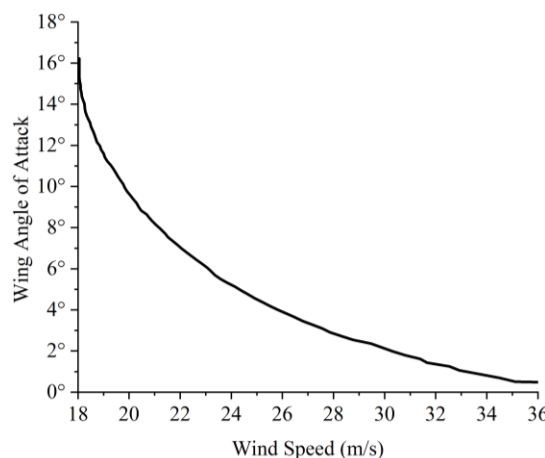


Figure 5. Wing angle of attack at various wind speeds to stay afloat.

$$\begin{aligned} F_{EB} &= Vg(\rho_s - \rho_{eb}) \\ &\approx 600 \times 9.81 \times (0.8 \\ &\quad - 0.179) N \approx 3750 N \end{aligned} \quad \boxed{\text{Equation 5}}$$

The aerodynamic lift component is generated by the wing structures affixed to each energy unit. These wings are designed based on the NACA 4412 airfoil series, whose performance characteristics were sourced from [46]. Importantly, the data were extracted at the appropriate Reynolds numbers.

Lift Generation Across Angles of Attack

Figure 5 illustrates how the lift generated by the wings varies with

$$F_{AF} = \frac{1}{2} \rho V^2 A_c C_l \quad \boxed{\text{Equation 6}}$$

different angles of attack. The lift force, F_{AF} , can be described by the **Equation 6** where ρ is the air density, V is the wind velocity, A_c is the wing area, and C_l is the coefficient of lift. To maintain a constant lift force of 17,167 N, required for stable operation, the wings dynamically

adjust their angle of attack as a function of wind speed. If wind speeds were to fall below 18 m/s, the system's capacity for dynamic angle of attack adjustment allows for crosswind operation, serving as a fail-safe to maintain altitude. Such instances are deemed to be rare events, less than 8%.

4 VAWT Cluster

The present SkyWindFarm model features an innovative cluster of four VAWTs per Energy Unit, as depicted in **Figure 6**. To identify the most optimal configuration for the Vertical Axis Wind Turbine VAWT cluster, multiple designs underwent rigorous testing. Detailed information on these designs is available in Appendix 1.

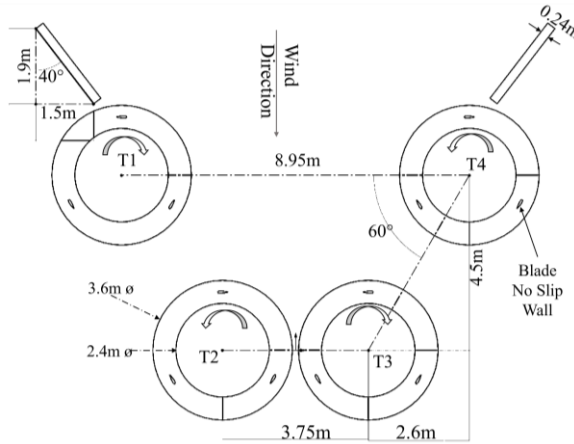


Figure 6 Enlarge view of layout of turbine's rotating domain with dimensions.

Table 1: List of denominations and their values

Denomination	Value
Turbine Diameter	3 m
Considered Region Diameter	15 m
Turbine Height	4 m
Airfoil Chord Length	0.3 m
Tip Speed Ratio	3
Solidity	0.3

4.1 CFD Simulation

This current configuration aims to overcome some of the inherent challenges in VAWT performance while maximizing efficiency. The simulation framework for the design comprises of mesh settings, solver configurations, and performance metrics, as detailed in the subsequent sections. The design features a three bladed wind turbine utilizing the NACA 0021 airfoil. The turbine specifications are given in **Table 1**.

Diffuser Walls

One limiting factor in the performance of traditional VAWTs is the negative torque experienced during the airfoil's return revolution. This negative torque diminishes the overall power output of the turbine. To mitigate this, SkyWindFarm employs a diffuser-augmented arrangement, wherein a diffuser wall is strategically placed inspired by [47] as shown in **Figure 6**. This wall blocks air from striking the turbine blades at negative angles while simultaneously accelerating air that encounters the blades at advantageous angles.

Computational Setup

The computational setup delineates the design and spatial configurations crucial for the analysis. **Figure 6** offers a detailed perspective of the turbines, accentuating the dimensions pertinent for the study. The boundary conditions for the computational domain are defined, with designated “Velocity Inlet” of 26.7m/s and atmospheric pressure at 3000 meters for “Pressure Outlet” regions complemented by the

peripheral boundaries labeled as “Boundary 1” and “Boundary 2” in **Figure 7**, where the distance from the boundary walls is represented in terms of the turbine diameter. In the computational model, a cylindrical rotating domain with an inner diameter of 2.4 meters and an outer diameter of 3.6 meters was established to simulate the rotational motion of the turbine. The surfaces of the airfoil blades were designated as no-slip walls, assuming no deformation, to accurately reflect the boundary conditions encountered in physical operation.



Figure 8a – Meshing Picture for the CFD

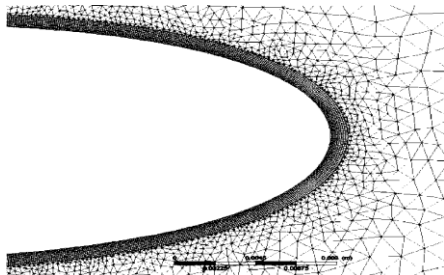


Figure 8b – Mesh zoomed in near an Airfoil of turbine.

method [48], [49], [50], [51]. The SIMPLE algorithm is utilized for the semi-implicit method, with second-order spatial discretization for pressure, momentum, and turbulence equations. To capture the turbulence correctly, the SST $k-\omega$ turbulence model is adopted.

Equations 7 through 11 delineate the fundamental fluid dynamics and turbulence characteristics within the computational domain. They are iteratively solved over each discrete volume element within the mesh to ensure the conservation of mass, momentum, and energy throughout the simulated flow field. This iterative process advances in time steps, refining the solution to a converged state that accurately reflects the transient behavior of the physical system under investigation. In the conservation equations (7 and 8), the fluid density is ρ and u_i, u_j are the velocity components in the flow field. Pressure is P , while μ and

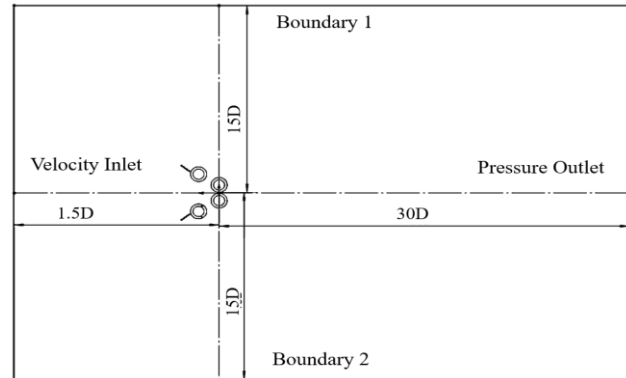


Figure 7. Computational Setup (layout of air flow)

Mesh Settings

An isometric view in **Figure 8a** reveals the spatial layout and arrangement of the turbines in a three-dimensional setting. The simulation employs a sliding mesh model to capture the unsteady flow dynamics induced by the rotating turbine blades as shown in **Figure 8a**. ANSYS Meshing is used to generate a non-conformal mesh with unstructured quadrilateral and prism elements. The mesh is further refined near the airfoil surfaces to account for the boundary layer, featuring 10 levels of quadrilateral elements with a maximum thickness of 2 mm and a growth rate of 1.1. The $y+$ value for the mesh falls within the range of 1 to 5, and the mesh consists of 3,057,836 elements.

Solver Settings

Fluent code is employed to solve the unsteady Reynolds-averaged Navier-Stokes equations using the finite volume

μ_t denote molecular and turbulent viscosity, respectively. Equations 9 and 10 are turbulence modeling equations where turbulent kinetic energy is k , and its rate of dissipation is ω . The symbol P_k stands for the production of k , and f_i represents body forces. Model constants α , β , β^* , σ_k , σ_ω , and $\sigma_{\omega2}$, along with blending functions F_1 and F_2 , enable the model to adapt from wall to free-stream behavior. In equation 11 for kinematic eddy viscosity, v_T , links turbulence to mean flow.

The Reynolds number for the flow is approximately 6×10^6 which is ideal for the selected turbulence model. Initially, a steady-flow simulation is conducted to establish reasonable parameters for the flow domain. This is followed by unsteady flow simulations using the Sliding Mesh Model (SMM). A time step size, corresponding to a turbine rotation of 1.0 degree, is used for the time-dependent solution [52], [53], [54]. Convergence criteria include a drop of at least three orders of magnitude in residuals for each time step and a minimum of 20 iterations per time step. The combined batch run took just under an hour to compute on the Agate A100 GPU cloud cluster with 128 cores per node.

Continuity	$\frac{\partial \rho}{\partial t} + \frac{\partial}{\partial x_j}(\rho u_j) = 0$	Equation 7
Momentum	$\frac{\partial}{\partial t}(\rho u_i) + \frac{\partial}{\partial x_j}(\rho u_i u_j) = -\frac{\partial p}{\partial x_i} + \frac{\partial}{\partial x_j} \left[(\mu + \mu_t) \left(\frac{\partial u_i}{\partial x_j} + \frac{\partial u_j}{\partial x_i} - \frac{2}{3} \frac{\partial u_k}{\partial x_k} \delta_{ij} \right) \right] + f_i$	Equation 8
Turbulence Kinetic Energy (k)	$\frac{\partial k}{\partial t} + U_j \frac{\partial k}{\partial x_j} = P_k - \beta^* \rho \omega k + \frac{\partial}{\partial x_j} \left[(v + \sigma_k v_t) \frac{\partial k}{\partial x_j} \right]$	Equation 9
Specific Dissipation Rate (ω)	$\frac{\partial \omega}{\partial t} + U_j \frac{\partial \omega}{\partial x_j} = \alpha S^2 - \beta \rho \omega^2 + \frac{\partial}{\partial x_j} \left[(v + \sigma_\omega v_t) \frac{\partial \omega}{\partial x_j} \right] + 2(1 - F_1) \sigma_{\omega2} \frac{1}{\omega} \frac{\partial k}{\partial x_j} \frac{\partial \omega}{\partial x_j}$	Equation 10
Kinematic Eddy Viscosity	$v_T = \frac{a_1 k}{\max(a_\omega, SF_2)}$	Equation 11

Results of CFD simulation

The velocity contour on SkyWindFarm is shown in **Figure 9**. The torque coefficient (C_m) and the coefficient of power (C_p) are calculated using **Equations 12 and 13**, where T_s is the total torque on the blade surface, V_∞ is the free stream velocity,

R is the turbine radius, and A_s is the surface area of the blade. The **Figure 10** demonstrates the average Tip Speed Ratio (TSR) for each

$C_{ms} = \frac{T_s}{0.5 \rho V_\infty^2 R A_s}$	Equation 12
$C_p = C_m * \lambda$	Equation 13
$\lambda = \frac{\omega R}{V_\infty}$	Equation 14

turbine in the cluster. TSR was determined as per **Equation 14**, where λ denotes TSR, ω represents the angular velocity. It reveals that the average performance of each turbine

is significantly enhanced in this arrangement. Specifically, Turbines 1 and 4 outperform Turbines 2 and 3 due to the diffuser arrangement. Furthermore, the performance of Turbines 1 and 2 is superior to that of Turbines 3 and 4, mainly because Turbine 1 mitigates some of the negative torque affecting Turbine 2.

Notably, the overall optimal average C_p for the VAWT cluster is 0.46 at a TSR of 3.00. **Figure 11** shows the velocity streamlines for one of the turbines.

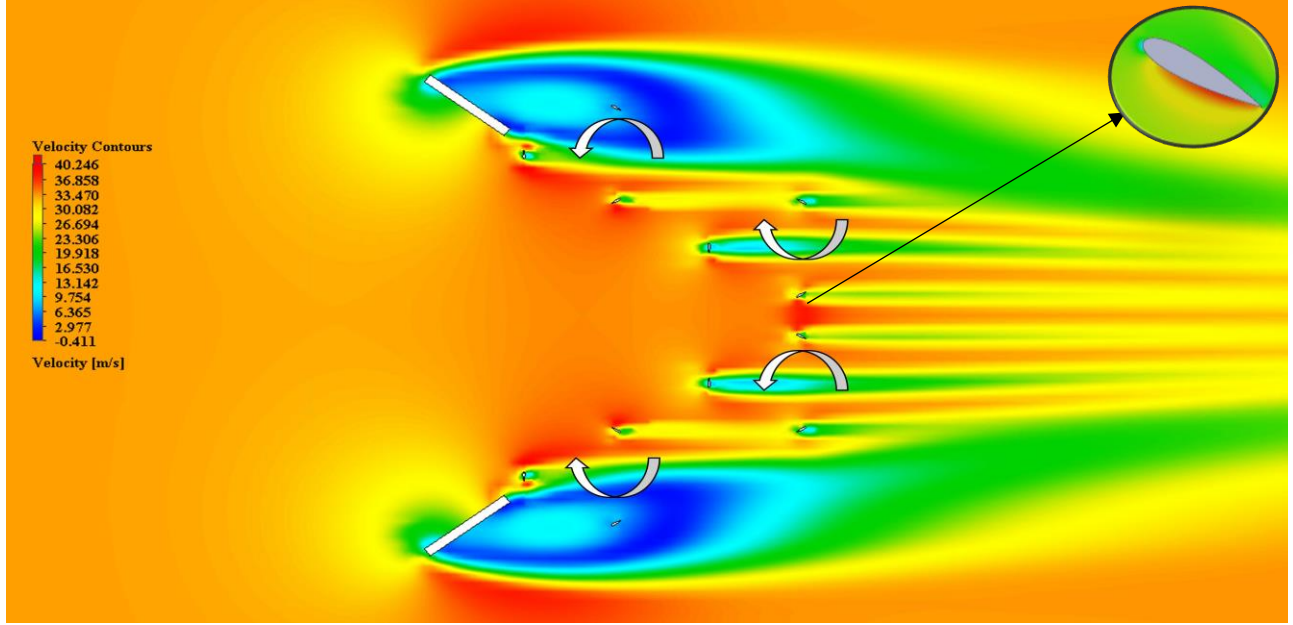


Figure 9. Velocity Contour on SkyWindFarm

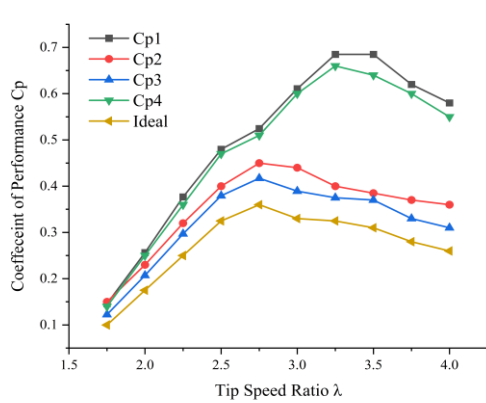


Figure 10 Tip Speed Ratio (TSR) v/s coefficient of power (C_p) of the proposed VAWT Cluster compared to an ideal VAWT.

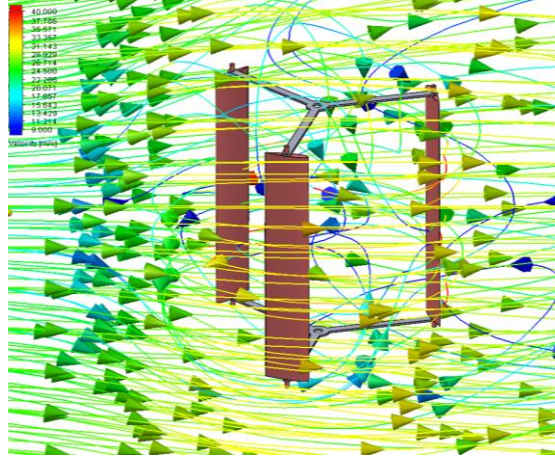


Figure 11 - Velocity Streamlines around an ideal turbine

4.2 Wind Tunnel Testing

Test Setup

The primary objective of the wind tunnel testing was to corroborate the CFD simulations concerning the aerodynamic behavior of the turbine cluster. To this end, a meticulously crafted lab-scale prototype, modeled at a 1:20 scale ratio, was employed, as depicted in **Figure 12a**. This prototype was constructed utilizing the Stratasys Objet 500 Rigur (RGD45) resin, selected for its superior tensile strength and its capacity to provide a smooth finish—attributes that are essential for precise aerodynamic experimentation.



Figure 12a. Lab scale fully functioning prototype



Figure 12b. Wind Tunnel Testing Struct



Figure 12c. Wind Tunnel Testing Setup

For the purposes of the tests, a consistent wind velocity of 26.7 m/s was upheld to ensure the establishment of fully turbulent flow conditions, achieved at a Reynolds number (Re) equal to or exceeding $Re \geq 5 \times 10^4$. Under these conditions, the turbine models were subjected to an operational $Re = 3 \times 10^5$, which lies within the turbulent regime necessary for reliable data extrapolation to full-scale scenarios. This regime was facilitated by the capabilities of the Large CR Tunnel, featuring a maximum flow speed of 38 m/s (85 mph), a cross section of 1 x 1.25 m, and a 100 HP, frequency-controlled variable speed motor driving a P-38 Feathering Propeller. During the testing phase, the structures were meticulously designed to provide ample open space, facilitating the routing of electrical cables necessary for measuring power output and adjusting resistance in real time, as illustrated in **Figure 12b**. A thorough structural analysis was conducted to ensure that the turbines maintained their shape. The wind tunnel testing setup is depicted in **Figure 12c**.

The scale-independent performance metrics, namely TSR and C_p , were meticulously evaluated. A tri-phase generator was implemented to quantify the power output, and C_p was determined by the ratio of harvested power to the total power available across the turbine's cross-sectional area as **Equation 13**. The TSR was modulated by varying the resistance encountered by the turbines during the power measurement phase, thereby enabling the precise adjustment of TSR to the desired values. The power was straightforwardly computed by multiplying the voltage by the current. Markers were strategically placed on the turbine blades to assist with the post-test analysis of rotational velocity, and high-speed video

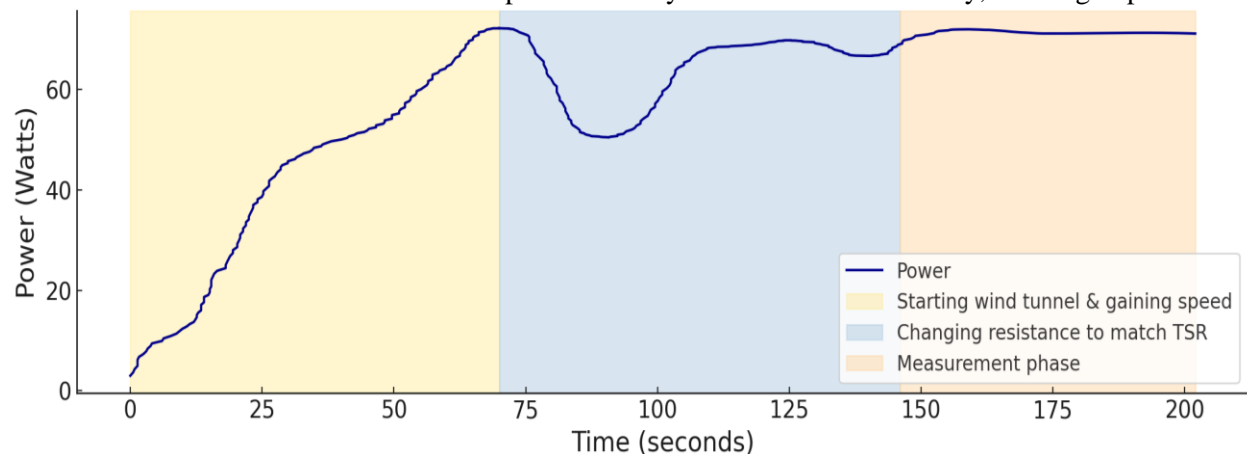


Figure 13. Wind Tunnel Power Measurement

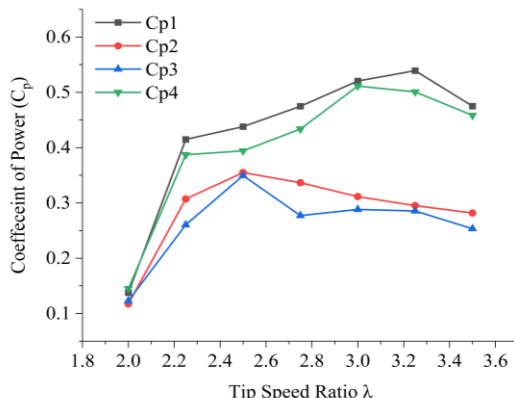


Figure 14. TSR VS CP

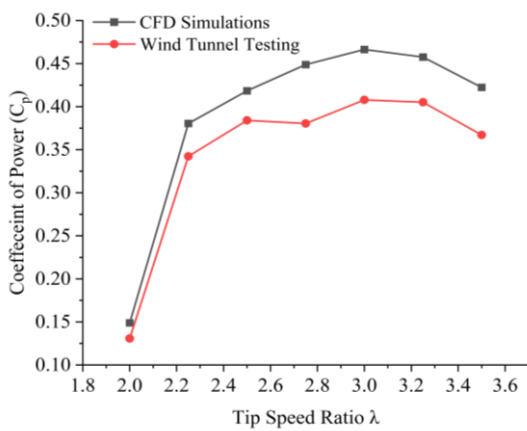


Figure 15 - Average TSR vs CP for wind tunnel testing vs CFD simulations

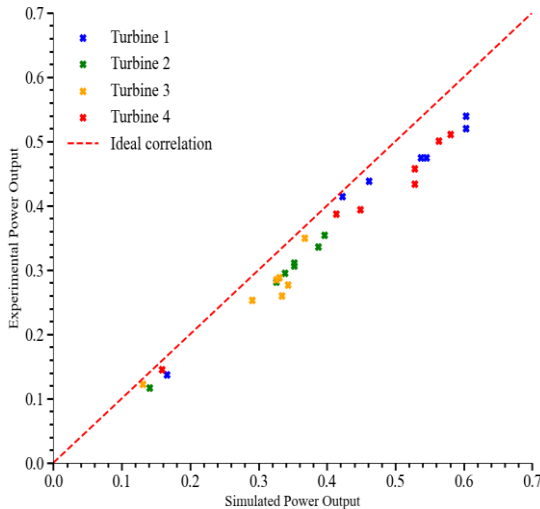


Figure 16. correlation plot of simulated and experimental power outputs results of all turbines.

recording at 240 frames per second was utilized to ensure an accurate assessment of TSR under varying resistance conditions.

Results of wind tunnel testing

Figure 13 delineates three distinct phases of the testing procedure. The initial phase, shaded in light yellow, represents the wind tunnel's start-up sequence, where the wind speed ramps up to the target testing velocity and the power produced increases. The second phase, highlighted in blue, illustrates the period of adjusting the resistance to match the desired TSR values, ensuring that it is within the optimal range for performance testing. As can be seen, the power fluctuates quite a bit as TSR changes. Finally, the measurement phase, shaded in peach, captures the steady-state operation where the power output stabilizes. It is during this phase that the most critical and relevant data for validating the CFD simulations are captured.

In the interest of maintaining structural integrity and minimizing vibrational effects, dual linear reinforcement plates of minimal thickness were incorporated at the turbine's midpoint. Testing was executed across Tip Speed Ratios (TSRs) ranging from 2 to 3.5, in increments of 0.25. The subsequent **Figure 14** delineates the relationship between TSR, and the Coefficient of Performance (Cp) as observed during wind tunnel experimentation.

The experimental results demonstrated good alignment with the CFD simulations. Mean power outputs between the simulated and wind tunnel data showed strong agreement, with the latter being marginally lower due to real-world inefficiencies, mainly the generator inefficiency, as can be seen in **Figure 15**.

Correlation coefficients exceeded 0.95 for all turbines, indicating a robust linear relationship between the simulated and experimental datasets as can be seen in **Figure 16**.

4.3 Total Power Produced by an Energy Unit

The cumulative power output for a single Energy Unit in this configuration was determined by using the Average CP of the physical testing and the CFD simulations is 0.43 at TSR of 3.00. Based on these models, the average power was calculated to be 157 kW, as can be seen in **Equation 15**, where C_p is the coefficient of power, C_A is the cross sectional area and N_t is the number of turbines. It is imperative to account for auxiliary losses in order to accurately estimate the net power output of an Energy Unit. These losses primarily stem from the generator and tether systems, each exhibiting a conservative efficiency of approximately 90% [26], [55]. The comprehensive power output, factoring in these efficiencies, can be mathematically expressed as shown in **Equation 16**, where $P_{harvested}$ is the power harvested by the Energy Unit, μ_T is tether efficiency at flying altitude of 3km, μ_G is generator efficiency.

$P_{harvested} = 0.5\rho V^3 C_p C_A N_t$ = $0.5(0.8)(26.7^3)(0.43)(12)(4)$ = 157.146 kW	<i>Equation 15</i>
$P_{EU} = P_{harvested} \mu_T \mu_G$ ≈ $157 * 0.90$ * 0.90 = 127 kW	<i>Equation 16</i>

5 Stability

SkyWindFarm incorporates an aerodynamically optimized Lighter-Than-Air (LTA) shell to facilitate rapid adjustments to wind disturbances. This section delineates the methodology and findings of the Dynamic Stability Analysis conducted to evaluate the system's robustness against abrupt wind direction changes.

5.1 Computational Domain and Mesh Settings

The computational domain for the stability analysis included 2,079,065 cells. A non-conformal mesh with unstructured quadrilateral and prism elements were employed, akin to the mesh settings used in the VAWT

cluster simulations. The geometry was simplified by removing the bridle system and the generators from the computational domain. Everything else was treated as a no slip wall with zero deformation. The $y+$ around the Energy Unit surfaces was between 1 and 5.

5.2 Solver and Turbulence Model

The simulation employed the Fluent code to solve the unsteady Reynolds-averaged Navier-Stokes

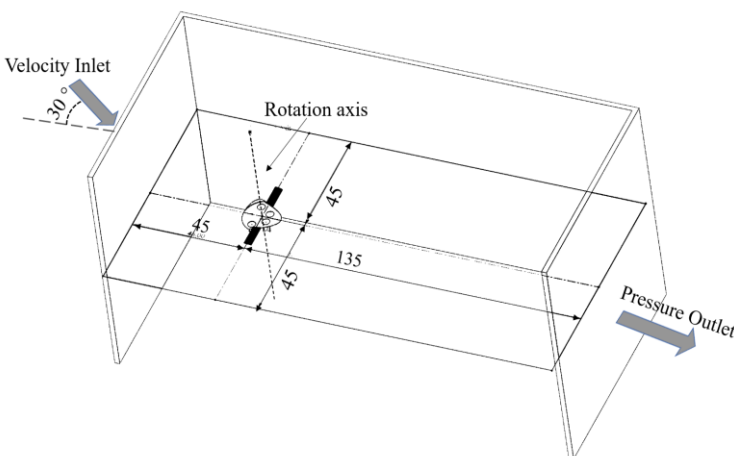


Figure 17. Isometric view of computational domain setup for stability analysis

(RANS) equations using the finite volume method, consistent with the VAWT cluster simulation. The Semi-Implicit Method for Pressure-Linked Equations algorithm was utilized with a second-order spatial discretization for all pressure, momentum, and turbulence equations. Gradients were calculated using the Least Squares Cell-Based algorithm. Once again, the Shear-Stress Transport $k - \omega$ (SST $k - \omega$) turbulence model was adopted, as shown Equations 7-11, for capturing the turbulence characteristics accurately as the Reynolds number was quite high.

5.3 Simulation Protocol

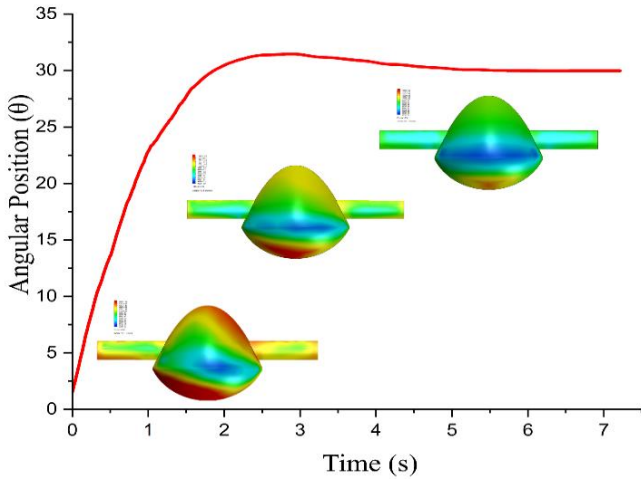


Figure 18. Change in wind direction with time vs angular position.

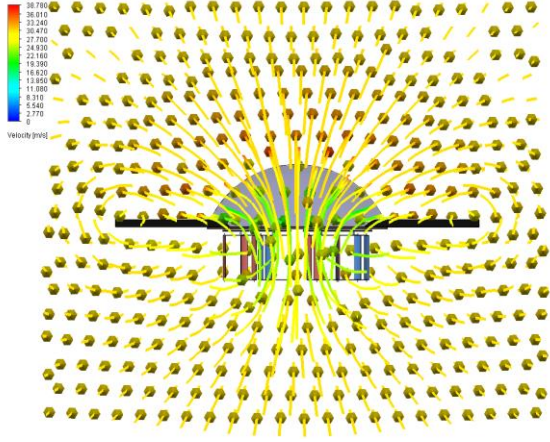


Figure 19. Flow Streamlines over SkyWindFarm at 9s time.

The stability of the SkyWindFarm was evaluated using a 6 Degrees-of-Freedom (DOF) simulation method with one axis rotation enabled. **Figure 17** shows the isometric view of computational domain setup for stability analysis. The objective was to assess the system's dynamic stability against abrupt changes in wind direction, specifically a sudden 30-degree shift in wind velocity. The total lift and drag forces exerted on the surface of the Energy Unit were calculated, enabling the determination of the aggregate lift and drag forces as well as the location of the center of pressure. Initially, a steady-state simulation was conducted to establish baseline flow domain parameters. This was followed by transient simulations incorporating the full 6 DOF model to capture the unsteady dynamics. Convergence criteria for the transient simulation were defined as a residual drop of at least three orders of magnitude, with a minimum of 20 iterations performed per time step. The computational simulation was set to a time step of 0.005 seconds and ran for a total of 2500 time steps, which corresponds to simulating 12.5 seconds of real-world time. This process required 14 minutes of computation time when executed on the Agate A100 GPU cloud cluster node, which boasts 128 cores per node. **Figure 18** shows graph of the change in wind direction with time and angular position of farm, and **Figure 19** shows flow trajectories over sky wind farm at 9 seconds' time.

5.4 Result of stability analysis

The stability analysis revealed that SkyWindFarm could reorient itself to face the new wind direction within a duration of only 7.2 seconds, as indicated in **Figure 20**. This swift reorientation highlights the system's resilience and adaptability to sudden wind changes, vital for maintaining consistent energy generation and overall safety.

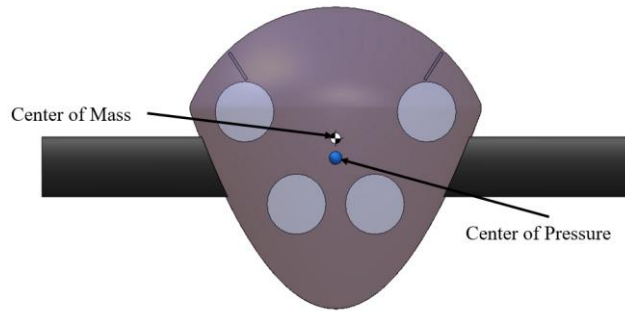


Figure 20. Center of Pressure vs Center of Mass for the system

this spatial arrangement, revealing that the center of pressure remains behind the center of mass even at the system's maximum angle of attack. This inherent design feature contributes to SkyWindFarm's self-righting capabilities, enabling the system to recover effectively from abrupt wind disturbances.

6 Field Testing for the Energy Unit

6.1 Objective and Setup

The primary objective of the field testing was to validate the operational stability of the SkyWindFarm Energy Unit at high altitudes. A fully functional model of the Energy Unit, featuring a power output capacity of 0.20 kW, was constructed and tested. The unit comprised four contra-rotating wind turbines and utilized two 15-foot hydrogen balloons for lift, as shown in **Figure 21**. It's important to note however that The ratio of the LTA shell the to turbines is a square cube relationship. For a 1:15th scale prototype the ratio is quite large. However, a 15m x 15m SkyWindFarm will have much more optimal ratio only requiring one aerodynamic enclosure.

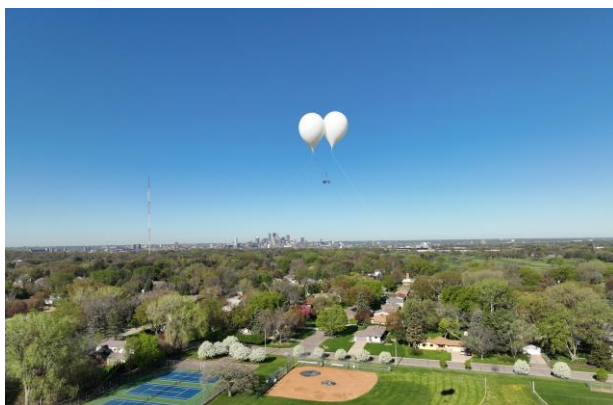


Figure 21 – Two balloons lifting Energy Unit up to 150 meters



Figure 22 – Tethers connecting the Energy Unit demonstrating how it is free to rotate.

For the test, the model was suspended in a manner that allowed free rotation with the wind direction, simulating real operational conditions as shown in **Figure 22**. The unit weighed 8.1 kg. Testing was conducted in the early morning under wind conditions ranging from 5-7 m/s, as measured by an onboard anemometer with a resolution of 0.05 m at a frequency of 1 Hz.

6.2 Control System and Power Optimization

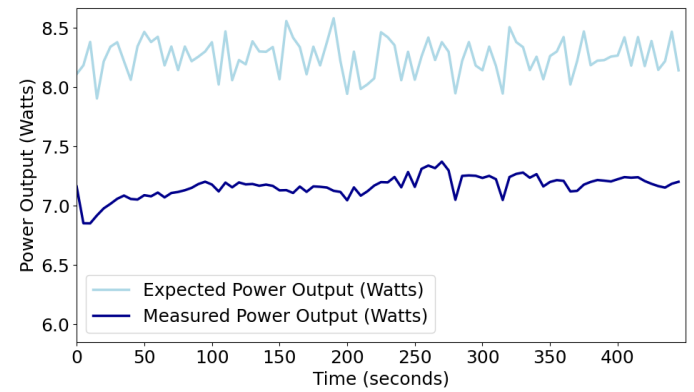
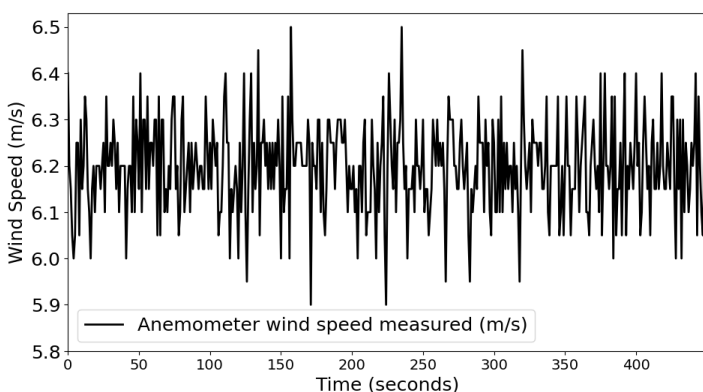
An onboard computer controlled a generator with a variable resistor, designed to optimize the Tip Speed Ratio based on the CFD optimizations conducted in section 4. The control algorithm calculated expected power output, as shown in **Equation 15**, and adjusted the resistance dynamically to harness maximum power. This adjustment occurred every three seconds, based on the average wind speeds recorded during the previous cycle.

6.3 Results and Observations

The field test duration was 37 minutes, with an initialization period of 15 minutes for the control algorithm. A significant observation window of 7 minutes and 30 seconds featured the most stable wind conditions, where average wind speeds were recorded at 6.2 m/s, and the average power output was 7.16 watts. The wind speeds and power output measurements can be seen in **Figure 23** and **Figure 24**. Test results showed that the operational efficiency was approximately 86% of the CFD predicted values.

The reduced power output can be attributed to the conservative response rate of the control algorithm and the effect of scaling down the prototype, which significantly lowered the Reynolds number by a factor of 100. At this lower Reynolds number, airfoils typically produce less lift and experience higher drag, leading to reduced efficiency. However, it is anticipated that as the scale of the prototype increases, the efficiency will also significantly improve.

Importantly, the prototype demonstrated excellent stability; there was no negative torque observed, and the turbines effectively canceled out each other's torques, leading to smooth operations even when the altitude of the Energy Unit was varied. The results confirm the system's potential for stable, efficient performance at scale in various wind conditions.



7 Cost Analysis

SkyWindFarm's design exhibits inherent scalability. Additional Energy Units could be added to an existing system while encountering minimal logistical challenges, primarily due to the copious availability of airspace and the system's operational flexibility across a range of altitudes. Consequently, the power output of SkyWindFarm can be dynamically adjusted to meet varying demand levels. The scalability and

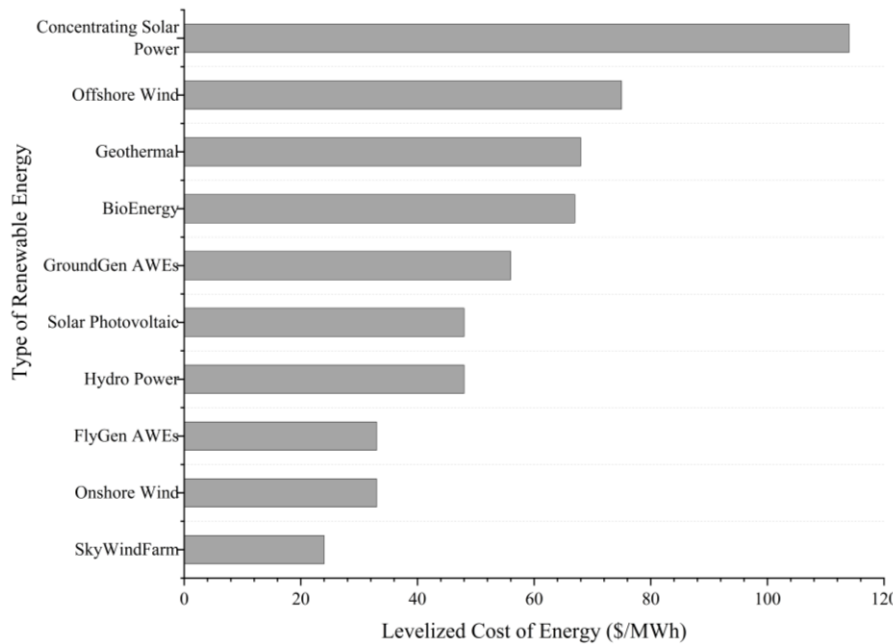


Figure 25. LCOE for Various Different Renewable Energy Sources

its economic implications have been analyzed, drawing on resources [45], [56], [57] for an in-depth cost assessment.

In conducting the cost analysis for SkyWindFarm, a novel system without existing financial models, National Renewable Energy Laboratory (NREL) protocols [58] are adapted to ensure rigor and standardization. The analysis assumes tether,

generator, and LTA shell costs to be similar to other AWEs, reflecting comparable operational characteristics. Given AWEs' minimal land use, this aspect is considered negligible. Salvage values are calculated at 15% of the original cost, integrating realistic lifecycle considerations.

The cost analysis herein is predicated upon an annual production rate of 250 Energy Units per year after an initial production phase of 150 Energy Units, aligning with standard values posited by the NREL. London has been selected as the operative locale for this analysis. Referencing **Figure 1**'s probability density function, it is projected that SkyWindFarm will maintain an operational uptime of 90% within the optimal wind speed parameters of 18 to 33m/s, which represent the system's cut in and cutout wind speeds, respectively. To account for maintenance requisites and meteorological contingencies, an additional 10% operational downtime is presupposed, yielding an aggregate capacity factor of 81%. The resultant life cycle energy yield of the farm is estimated at approximately 22,000 MWh, which incorporates the variability inherent in local wind speed distributions.

Life-limited elements, such as the tether and bridle line system, are forecasted to possess a functional span of 10 years, while the overarching infrastructure is projected for a 20-year lifespan. It is postulated that

helium or hydrogen attrition within the LTA shell will necessitate a comprehensive system replenishment biennially. This assumption is predicated on cumulative leakage over a 24-month period, equating to a full system restoration.

The Capex cost for each VAWT coupled with a PMDD generator, is estimated at \$15,000, encompassing both component costs and installation fees. Grid integration and regulatory compliance are projected to incur an additional \$150,000, with a further \$50,000 allocated for maintenance and component replacements. Given SkyWindFarm's minimal land usage requirements and the compatibility of the surrounding area for agricultural activities, leasing expenditures are substantially reduced compared to conventional systems. Thus, the total life cycle cost of SkyWindFarm over a 20-year period is calculated to be approximately \$540,000 correlating to an levelized cost of energy (LCOE) of roughly \$25/MWh.

The comparison depicted in **Figure 25** illustrates SkyWindFarm's competitive edge in the wind energy market. The data for all the renewable energy resources was taken from [59]. The data for Groundgen and Flygen AWEs was taken from [45].

Not only does SkyWindFarm undercut the cost of traditional fossil fuel-based energy, but it also demonstrates a roughly 25% improved cost-efficiency over existing flygen-based AWEs, with an LCOE of \$33/MWh. It is imperative to recognize that these cost metrics are highly contingent upon the specific location, operational altitude, and local wind speed profiles. In some regions, the associated costs could be markedly lower or higher. A principal factor underpinning the superior cost-efficiency of SkyWindFarm relative to traditional energy sources is the reduced material consumption. **Figure 26**, drawn to scale, shows the comparison between a conventional 150kW wind turbine [60] and the SkyWindFarm configuration.

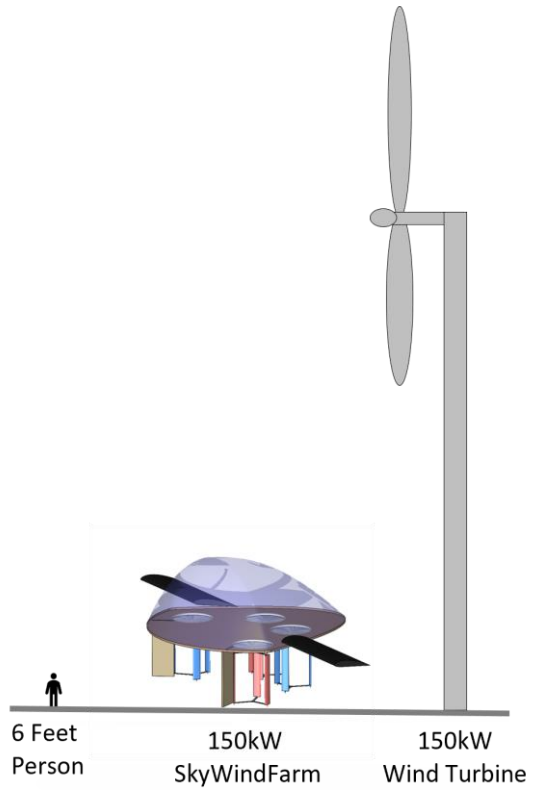


Figure 26. Comparative Scale Illustration of the SkyWindFarm and a Conventional 150kW Wind Turbine

7.1 Impact

The adoption of renewable energy solutions is often perceived as being primarily hindered by the initial costs associated with their production. However, a more significant limitation lies in their scalability and operational flexibility across diverse regions, as shown in **Figure 27**. [61], [62] To truly enhance the penetration of renewable energies, it is essential to develop systems that are not only economically viable but also capable of functioning effectively in varied geographical and environmental conditions. The need for renewable

technologies to be adaptable and scalable underscores the importance of innovative approaches that can mitigate the geographical limitations currently facing traditional renewable systems.

One of the prominent challenges in integrating renewable energy sources into the power grid is managing the so-called 'duck curve'—a phenomenon that occurs due to the variability in renewable energy supply.[63] Further, current renewables are inherent unpredictable and depend on weather conditions, which can lead to significant disparities in energy production and demand. Consequently, there is a continuous requirement for robust energy storage solutions to ensure stability and reliability in the energy grid.[64] The intermittency of renewable sources necessitates substantial investments in storage technologies, which can retain excess energy generated during peak production periods and release it during low production times.

Systems, such as SkyWindFarm, that transcend these conventional limitations by operating beyond specific regional confines present a promising avenue for the expansion of renewable energy applications.

8 Conclusion

The present study has introduced the SkyWindFarm design, a novel high-altitude wind energy system, designed to harness the powerful winds found at high altitudes. The study addresses key challenges and their corresponding mitigation strategies. The comprehensive theoretical framework, bolstered by simulations and a fully functioning lab-scale prototype, has underscored the feasibility and efficacy of this system, elevating it to a Technology Readiness Level (TRL) of 5.

SkyWindFarm presents a viable solution for remote communities seeking a reliable power source. Its ease of setup and minimal component requirement facilitate rapid deployment, making it an accessible energy alternative.

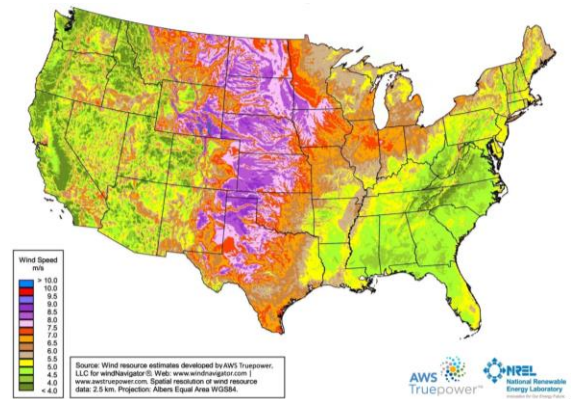


Figure 27 - Annual average wind speeds at 80m in the United States [61]

8.1 Key Findings

- **Harnessing High-Altitude Winds:** By targeting high altitude winds and sub-tropical jet streams, which exhibit enormous energy and persistence, SkyWindFarm aims to exploit a resource that offers two orders of magnitude greater potential annual energy output than equivalent ground-based turbines. The jet streams, with average velocities around 130 km/h, present a remarkable opportunity for renewable energy capture.
- **Aerodynamic and Structural Design:** Numerical analyses and CFD simulations have been employed to optimize the aerodynamic design, resulting in a stable and robust configuration.
- **Robustness and Adaptability:** The two-way lift method, featuring a helium balloon and an adjustable airfoil wing, ensures operational stability even under varying wind conditions.
- **Wind Tunnel Testing and Validation:** Rigorous wind tunnel testing has been pivotal in validating the design's aerodynamics and structural integrity.
- **Field Testing Validation:** Field tests have demonstrated the system's ability to operate efficiently and stably at high altitudes, confirming its practical viability and alignment with CFD predictions, and establishing a firm groundwork for scaling up the prototype.
- **Cost Analysis:** A detailed cost analysis reveals SkyWindFarm's economic viability, highlighting its 25% cost advantage over existing AWEs.
- **Technology Readiness:** The project has successfully achieved TRL 5, indicating significant progress in technology validation.

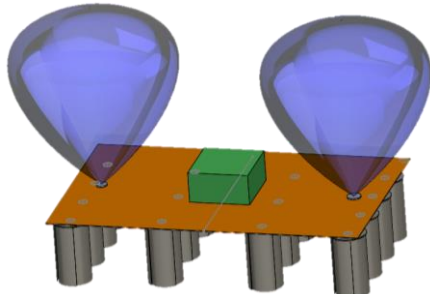
In conclusion, the SkyWindFarm design represents a groundbreaking advancement in the field of renewable energy. By tapping into the immense energy potential of high-altitude winds, it offers a sustainable and inexhaustible power source. The theoretical modeling, comprehensive numerical analysis, and practical simulations conducted in this work lay a solid groundwork for future development and implementation. With its scalability, SkyWindFarm can transition from powering small remote communities to multi-megawatt setups capable of supporting large communities, marking it as a versatile and efficient solution in the renewable energy landscape.

Appendix I

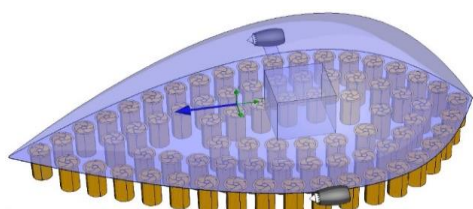
Design Iterations and Rationale Behind the Current Design

Design Iterations

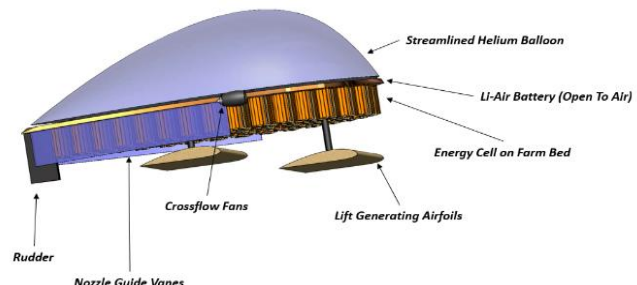
The initial design of SkyWindFarm of two hot air balloons as shown in **figure a**. However, the calculation of the coefficient of drag was found to be over 0.67 Newtons and the auxiliary power needed to maintain the system in place was unsuitable for practical use. To decrease the drag and improve the overall efficiency of the system, a new design was explored using streamlined balloon shape. This inspired design looked promising because of its airfoil like shape while some of the other perks of this design included a reduction in unwanted rotation and toppling. However, the main problem with these designs was the efficiency of turbines in the back rows was significantly lower than the front row turbine efficiency. These designs lead me to explore a 6 cluster VAWT Farm, before eventually landing on the current design.



Iteration 1 - Design iterations for the wind farm.



Iteration 2 - Streamlined balloon shape SkyWindFarm with multiple small turbines.



Iteration 3 - Streamlined balloon shape with nozzle guide vanes and Lift generating airfoil wings below the farm.

Testing Iterations

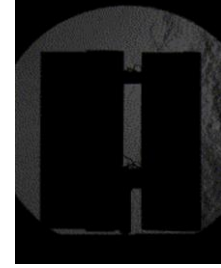
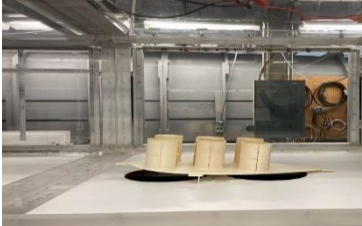
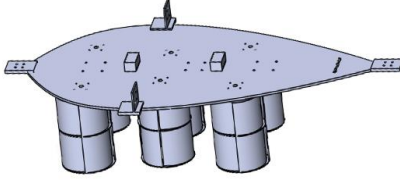
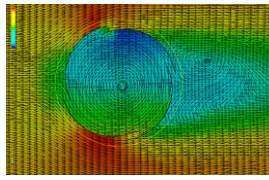
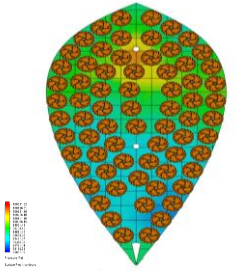
During the testing phase, multiple wind turbine prototypes were developed and evaluated, each named in honor of renowned scientists: **Gauss, Pythagoras, Turing, Euclid, and Newton**.

Gauss, the initial prototype, consisted of six energy cells. However, it exhibited suboptimal performance in the back row turbines. To address this, **Pythagoras** was developed as a smaller scale model of **Turing** which incorporated a six-turbine cluster with guide vanes, aiming to enhance overall efficiency. While Turing showed improved performance in the wind tunnel testing, the gain was not proportional to the increase in mass. **Euclid**, the third prototype, featured a four-turbine configuration to tackle the efficiency issue of back row turbines. Despite the addition of guide vanes, the increase in performance did not compensate for the added mass.

The final prototype, **Newton**, as depicted in **Figure 12a**, successfully resolved this challenge. It integrated diffuser walls that not only enhanced performance but also reduced mass, marking a significant advancement in the design.

Analysis Iterations

Schlieren imaging analysis is used to understand the Darrius and Savanious types of turbines, since savanious may offer better TSR to Cp ratio. However, it was found that Darrius wind turbines offer greater wake structure hence they were used throughout the study.

		
<i>Schlieren image setup</i>	<i>Turing and Pythagoras Prototype scale</i>	<i>Schlieren Image of savanious turbine</i>
		
<i>Wind tunnel testing setup for Turing</i>	<i>Turing Cad Model</i>	<i>CFD Simulation of Omni Guide Vanes</i>
		
<i>Wind tunnel testing setup for Gauss</i>	<i>Prototype of 4 turbine Omni + Venturi Guide vanes</i>	<i>CFD Simulation Iteration 2 Streamlined balloon shape Farm with multiple turbines</i>

9 References

- [1] R. Adib REN, M. Eckhart Mohamed El-Ashry David Hales Kirsty Hamilton Peter Rae, and F. Bariloche, ‘Renewables 2019 Global Status Report’, *Resources*, vol. 8, no. 3, p. 139, 2019, Accessed: Jan. 20, 2023. [Online]. Available: <https://wedocs.unep.org/xmlui/handle/20.500.11822/28496>

- [2] S. Shafiee and E. Topal, ‘When will fossil fuel reserves be diminished?’, *Energy Policy*, vol. 37, no. 1, pp. 181–189, Jan. 2009, doi: 10.1016/J.ENPOL.2008.08.016.
- [3] B. E. Rittmann, ‘Opportunities for renewable bioenergy using microorganisms’, *Biotechnol Bioeng*, vol. 100, no. 2, pp. 203–212, Jun. 2008, doi: 10.1002/BIT.21875.
- [4] Y. Chisti, ‘Biodiesel from microalgae’, *Biotechnol Adv*, vol. 25, no. 3, pp. 294–306, May 2007, doi: 10.1016/J.BIOTECHADV.2007.02.001.
- [5] A. Cherubini, A. Papini, R. Vertechy, and M. Fontana, ‘Airborne Wind Energy Systems: A review of the technologies’, *Renewable and Sustainable Energy Reviews*, vol. 51, pp. 1461–1476, Nov. 2015, doi: 10.1016/J.RSER.2015.07.053.
- [6] T. Cherubini, ‘Kite Dynamics and Wind Energy Harvesting’.
- [7] M. Diehl, ‘Airborne wind energy: Basic concepts and physical foundations’, *Green Energy and Technology*, pp. 3–22, 2013, doi: 10.1007/978-3-642-39965-7_1/COVER.
- [8] M. L. Loyd, ‘Crosswind Kite Power’, *J. ENERGY*, vol. 4, doi: 10.2514/3.48021.
- [9] A. Cherubini Tutor and M. Fontana, ‘Scuola Superiore Sant’Anna Advances in Airborne Wind Energy and Wind Drones’.
- [10] I. Argatov, P. Rautakorpi, and R. Silvennoinen, ‘Estimation of the mechanical energy output of the kite wind generator’, *Renew Energy*, vol. 34, no. 6, pp. 1525–1532, Jun. 2009, doi: 10.1016/J.RENENE.2008.11.001.
- [11] U. Zillmann and P. Bechtle, ‘Emergence and economic dimension of airborne wind energy’, *Green Energy and Technology*, vol. 0, no. 9789811019463, pp. 1–25, 2018, doi: 10.1007/978-981-10-1947-0_1.
- [12] J. Heilmann and C. Houle, ‘Economics of pumping kite generators’, *Green Energy and Technology*, pp. 271–286, 2013, doi: 10.1007/978-3-642-39965-7_15.
- [13] P. Faggiani and R. Schmehl, ‘Design and economics of a pumping kite wind park’, *Green Energy and Technology*, vol. 0, no. 9789811019463, pp. 391–411, 2018, doi: 10.1007/978-981-10-1947-0_16.
- [14] L. Perkovicá, P. Silva, M. Ban, N. Kranjčevic, K. Kranjčevic’c, and N. D. Duicá, ‘Harvesting high altitude wind energy for power production: The concept based on Magnus’ effect’, 2012, doi: 10.1016/j.apenergy.2012.06.061.
- [15] Maciej Serda *et al.*, ‘Comparison of concepts for high-altitude wind energy generation with ground based generator’, *Uniwersytet śląski*, vol. 7, no. 1, pp. 409–417, 2005, doi: 10.2/JQUERY.MIN.JS.
- [16] G. A. Malinga and J. M. Niedzwecki, ‘Lightning field behavior around grounded airborne systems’, 2015, doi: 10.1016/j.renene.2015.10.047.
- [17] L. Fagiano, E. Nguyen-Van, F. Rager, S. Schnez, and C. Ohler, ‘Autonomous Takeoff and Flight of a Tethered Aircraft for Airborne Wind Energy’, *IEEE Transactions on Control Systems Technology*, vol. 26, no. 1, pp. 151–166, Jan. 2018, doi: 10.1109/TCST.2017.2661825.

- [18] M. Canale, L. Fagiano, and M. Milanese, ‘KiteGen: A revolution in wind energy generation’, 2008, doi: 10.1016/j.energy.2008.10.003.
- [19] M. Saeed and M. H. Kim, ‘Aerodynamic performance analysis of an airborne wind turbine system with NREL Phase IV rotor’, *Energy Convers Manag*, vol. 134, pp. 278–289, Feb. 2017, doi: 10.1016/J.ENCONMAN.2016.12.021.
- [20] A. Saleem and M.-H. Kim, ‘Effect of rotor axial position on the aerodynamic performance of an airborne wind turbine system in shell configuration’, 2017, doi: 10.1016/j.enconman.2017.09.026.
- [21] M. Saeed and M.-H. Kim, ‘Airborne wind turbine shell behavior prediction under various wind conditions using strongly coupled fluid structure interaction formulation’, 2016, doi: 10.1016/j.enconman.2016.04.077.
- [22] P. J. Sola, A. S. McDonald, and E. Oterkus, ‘A lightweight approach for airborne wind turbine drivetrains: European Wind Energy Association, EWEA 2015’. Nov. 19, 2015. Accessed: Aug. 07, 2023. [Online]. Available: <https://www.research.ed.ac.uk/en/publications/a-lightweight-approach-for-airborne-wind-turbine-drivetrains-euro>
- [23] C. Vermillion, B. Glass, and A. Rein, ‘Lighter-than-air wind energy systems’, *Green Energy and Technology*, pp. 501–514, 2013, doi: 10.1007/978-3-642-39965-7_30/COVER.
- [24] K. Geelen, J. Swevers, and M. Diehl, ‘Design and Operation of Airborne Wind Energy Systems.Experimental Validation of Moving Horizon Estimation for PoseEstimation’. Apr. 23, 2015. Accessed: Aug. 07, 2023. [Online]. Available: <https://lirias.kuleuven.be/1692956>
- [25] ‘Makani - X, the moonshot factory’. Accessed: Jul. 30, 2023. [Online]. Available: <https://x.company/projects/makani/#>
- [26] B. W. Roberts *et al.*, ‘Harnessing High-Altitude Wind Power’, *IEEE TRANSACTIONS ON ENERGY CONVERSION*, vol. 22, no. 1, 2007, doi: 10.1109/TEC.2006.889603.
- [27] C. G. Justus, W. R. Hargraves, A. Mikhail, and D. Graber, ‘Methods for Estimating Wind Speed Frequency Distributions’, *J Appl Meteorol Climatol*, vol. 17, no. 3, pp. 350–353, 1978, doi: [https://doi.org/10.1175/1520-0450\(1978\)017<0350:MFEWSF>2.0.CO;2](https://doi.org/10.1175/1520-0450(1978)017<0350:MFEWSF>2.0.CO;2).
- [28] Z. R. Shu and M. Jesson, ‘Estimation of Weibull parameters for wind energy analysis across the UK’, *Journal of Renewable and Sustainable Energy*, vol. 13, no. 2, p. 23303, Mar. 2021, doi: 10.1063/5.0038001/926742.
- [29] M. Wolsink, ‘Wind power implementation: The nature of public attitudes: Equity and fairness instead of “backyard motives”’, *Renewable and Sustainable Energy Reviews*, vol. 11, no. 6, pp. 1188–1207, Aug. 2007, doi: 10.1016/J.RSER.2005.10.005.
- [30] K. Pope, G. F. Naterer, I. Dincer, and E. Tsang, ‘Power correlation for vertical axis wind turbines with varying geometries’, *Int J Energy Res*, vol. 35, no. 5, pp. 423–435, Apr. 2011, doi: 10.1002/ER.1703.
- [31] L.-S. Shyu, *A pilot study of vertical-axis turbine wind farm layout planning*, vol. 953–954. 2014. doi: 10.4028/www.scientific.net/AMR.953-954.395.

- [32] S. Sahebzadeh, A. Rezaeiha, and H. Montazeri, ‘Towards optimal layout design of vertical-axis wind-turbine farms: Double rotor arrangements’, *Energy Convers Manag*, vol. 226, p. 113527, 2020, doi: 10.1016/j.enconman.2020.113527.
- [33] S. Dunker, ‘Tether and bridle line drag in airborne wind energy applications’, *Green Energy and Technology*, vol. 0, no. 9789811019463, pp. 29–56, 2018, doi: 10.1007/978-981-10-1947-0_2.
- [34] J. O. Dabiri, ‘Potential order-of-magnitude enhancement of wind farm power density via counter-rotating vertical-axis wind turbine arrays’, *Journal of Renewable and Sustainable Energy*, vol. 3, no. 4, Jul. 2011, doi: 10.1063/1.3608170/284824.
- [35] M. Shaheen and S. Abdallah, ‘Efficient clusters and patterned farms for Darrieus wind turbines’, *Sustainable Energy Technologies and Assessments*, vol. 19, pp. 125–135, Feb. 2017, doi: 10.1016/J.SETA.2017.01.007.
- [36] W. T. Chong, S. C. Poh, A. Fazlizan, and K. C. Pan, ‘Vertical axis wind turbine with omni-directional-guide-vane for urban high-rise buildings’, *J. Cent. South Univ*, vol. 19, 2012, doi: 10.1007/s11771-012-1064-8.
- [37] Y. C. Lim, W. T. Chong, and F. B. Hsiao, ‘Performance investigation and optimization of a vertical axis wind turbine with the omni-direction-guide-vane’, *Procedia Eng*, vol. 67, pp. 59–69, 2013, doi: 10.1016/J.PROENG.2013.12.005.
- [38] B. Shahizare, N. Nik-Ghazali, W. T. Chong, S. Tabatabaeikia, N. Izadyar, and A. Esmaeilzadeh, ‘Novel investigation of the different Omni-direction-guide-vane angles effects on the urban vertical axis wind turbine output power via three-dimensional numerical simulation’, *Energy Convers Manag*, vol. 117, pp. 206–217, Jun. 2016, doi: 10.1016/J.ENCONMAN.2016.03.034.
- [39] Y. A. Wicaksono, D. D. P. Tjahjana, and S. Hadi, ‘Influence of omni-directional guide vane on the performance of cross-flow rotor for urban wind energy’, *AIP Conf Proc*, vol. 1931, p. 30040, Feb. 2018, doi: 10.1063/1.5024099/FORMAT/PDF.
- [40] Y. Liu, B. Zwingmann, and M. Schlaich, ‘Carbon Fiber Reinforced Polymer for Cable Structures—A Review’, *Polymers 2015, Vol. 7, Pages 2078-2099*, vol. 7, no. 10, pp. 2078–2099, Oct. 2015, doi: 10.3390/POLYM7101501.
- [41] H. R. Pakravan and H. Yari, ‘The influence of nanostructured UV-blockers on mechanical properties of carbon fiber epoxy composites during accelerated weathering condition’, *Polym Adv Technol*, vol. 29, no. 2, pp. 970–981, Feb. 2018, doi: 10.1002/PAT.4208.
- [42] R. Bosman, V. Reid, M. Vlasblom, and P. Smeets, ‘Airborne wind energy tethers with high-modulus polyethylene fibers’, *Green Energy and Technology*, pp. 563–585, 2013, doi: 10.1007/978-3-642-39965-7_33/COVER.
- [43] V. Salma, F. Friedl, and R. Schmehl, ‘Improving reliability and safety of airborne wind energy systems’, *Wind Energy*, vol. 23, no. 2, pp. 340–356, Feb. 2020, doi: 10.1002/WE.2433.

- [44] A. M. Dokter, F. Liechti, H. Stark, L. Delobbe, P. Tabary, and I. Holleman, ‘Bird migration flight altitudes studied by a network of operational weather radars’, *J R Soc Interface*, vol. 8, no. 54, pp. 30–43, Jan. 2011, doi: 10.1098/RSIF.2010.0116.
- [45] H. Jannis, ‘The Technical and Economic Potential of Airborne Wind Energy CONTENTS’, 2012.
- [46] ‘NACA 4412 (naca4412-il) Xfoil prediction polar at RE=1,000,000 Ncrit=9’. Accessed: May 01, 2023. [Online]. Available: <http://airfoiltools.com/polar/details?polar=xf-naca4412-il-1000000>
- [47] T. G. Abu-El-Yazied, H. N. Doghiem, A. M. Ali, and I. M. Hassan, ‘Investigation of the aerodynamic performance of Darrieus vertical axis wind turbine’, *IOSR journal of engineering*, vol. 4, no. 5, pp. 18–29, 2014.
- [48] U. R. N. Cristobal, A. Gallegos-Mu??oz, and R. ??vila J. Manuel, ‘Numerical Analysis of a Rooftop Vertical Axis Wind Turbine’, *ASME 2011 5th International Conference on Energy Sustainability, ES 2011*, no. PARTS A, B, AND C, pp. 2061–2070, Mar. 2012, doi: 10.1115/ES2011-54173.
- [49] X. Sun, D. Luo, D. Huang, and G. Wu, ‘Numerical study on coupling effects among multiple Savonius turbines’, *Journal of Renewable and Sustainable Energy*, vol. 4, no. 5, Sep. 2012, doi: 10.1063/1.4754438/384330.
- [50] T. Zhou and D. Rempfer, ‘Numerical study of detailed flow field and performance of Savonius wind turbines’, *Renew Energy*, vol. 51, pp. 373–381, Mar. 2013, doi: 10.1016/J.RENENE.2012.09.046.
- [51] K. N. Morshed, M. Rahman, G. Molina, and M. Ahmed, ‘Wind tunnel testing and numerical simulation on aerodynamic performance of a three-bladed Savonius wind turbine’, *International Journal of Energy and Environmental Engineering*, vol. 4, no. 1, pp. 1–14, 2013, doi: 10.1186/2251-6832-4-18.
- [52] J. M. Edwards, L. Angelo Danao, and R. J. Howell, ‘Novel experimental power curve determination and computational methods for the performance analysis of vertical axis wind turbines’, *Journal of Solar Energy Engineering, Transactions of the ASME*, vol. 134, no. 3, Aug. 2012, doi: 10.1115/1.4006196/464821.
- [53] X. Sun, D. Luo, D. Huang, and G. Wu, ‘Numerical study on coupling effects among multiple Savonius turbines’, *Journal of Renewable and Sustainable Energy*, vol. 4, no. 5, Sep. 2012, doi: 10.1063/1.4754438/384330.
- [54] K. Kacprzak, G. Liskiewicz, and K. Sobczak, ‘Numerical investigation of conventional and modified Savonius wind turbines’, *Renew Energy*, vol. 60, pp. 578–585, Dec. 2013, doi: 10.1016/J.RENENE.2013.06.009.
- [55] G. L. Bywaters, E. Hancock, J. Tangudu, and L. Sethuraman, ‘Advanced Lightweight HiE PMDD Generator for WTGs’, Jul. 2022, doi: 10.2172/1893330.
- [56] ‘Levelized Cost of Energy Calculator | Energy Analysis | NREL’. Accessed: Nov. 03, 2023. [Online]. Available: <https://www.nrel.gov/analysis/tech-lcoe.html>
- [57] ‘CREST: Cost of Renewable Energy Spreadsheet Tool | Energy Analysis | NREL’. Accessed: Nov. 05, 2023. [Online]. Available: <https://www.nrel.gov/analysis/crest.html>

- [58] J. Weber *et al.*, ‘Airborne Wind Energy’, 2019, Accessed: Nov. 07, 2023. [Online]. Available: <https://www.nrel.gov/docs/fy21osti/79992.pdf>.
- [59] IRNEA, ‘IRENA (2022), Renewable Power Generation Costs in 2021, International Renewable Energy Agency, Abu Dhabi. ISBN 978-92-9260-452-3’, *International Renewable Energy Agency*, p. 160, 2022, Accessed: Nov. 03, 2023. [Online]. Available: https://www.irena.org/-/media/Files/IRENA/Agency/Publication/2018/Jan/IRENA_2017_Power_Costs_2018.pdf
- [60] ‘NORDTANK Wind Turbines 150kW XLR For Sale • MWPS World Wind Turbines’. Accessed: Nov. 03, 2023. [Online]. Available: <https://www.mwps.world/market/used-wind-turbines-offered/1kw-150kw-wind-turbines/used-wind-turbine-nordtank-150-kw-xlr-for-sale/>
- [61] D. Elliott *et al.*, ‘Abstract Methods Wind Potential: Key Findings 80 and 100 Meter Wind Energy Resource Potential for the United States 80 and 100 Meter Wind Energy Resource Potential for the United States’, 2010, Accessed: May 09, 2024. [Online]. Available: <http://www.awstruewind.com/windpotential.cfm>
- [62] ‘Overview and key findings – World Energy Investment 2023 – Analysis - IEA’. Accessed: May 09, 2024. [Online]. Available: <https://www.iea.org/reports/world-energy-investment-2023/overview-and-key-findings#clean-energy-spending>
- [63] R. Schmalensee, ‘Competitive Energy Storage and the Duck Curve’, *Energy Journal*, vol. 43, no. 2, pp. 1–16, Mar. 2022, doi: 10.5547/01956574.43.2.RSCH/SUPPL_FILE/SJ-PDF-1-ENJ-10.5547_01956574.43.2.RSCH.PDF.
- [64] J. Kosowatz, ‘Energy Storage Smooths the Duck Curve’, *Mechanical Engineering*, vol. 140, no. 06, pp. 30–35, Jun. 2018, doi: 10.1115/1.2018-JUN-1.